A Transmission Electron Microscopy study of composition in Si1-xGex / Si (001) quantum dots

Yidir Androussi, Tarik Benabbas, Slawomir Kret, Vincent Ferreiro, Alain Lefebvre

A Transmission Electron Microscopy study of composition in Si1-xGex / Si (001) quantum dots

Journal:	*Philosophical Magazine & Philosophical Magazine Letters*
Manuscript ID:	TPHM-06-Jun-0217.R1
Journal Selection:	Philosophical Magazine
Date Submitted by the Author:	27-Sep-2006
Complete List of Authors:	Androussi, Yidir; CNRS, LSPES UMR 8008 Benabbas, Tarik; CNRS, LSPES UMR 8008 Kret, Slawomir; Institute of Physics, Polish Academy of Sciences Ferreiro, Vincent; CNRS, LSPES UMR 8008 Lefebvre, Alain; CNRS, LSPES UMR 8008
Keywords:	quantum dots, transmission electron microscopy
Keywords (user supplied):	chemical composition, displacement field

Y. ANDROUSSI[1*], T. BENABBAS[1], S. KRET[2], V. FERREIRO[1] and A. LEFEBVRE[1]

[1] Laboratoire de Structure et Propriétés de l'Etat Solide (UMR CNRS 8008), Université des Sciences et Technologies de Lille, Bâtiment C6, 59655 Villeneuve d'Ascq cedex, France
[2] Institute of Physics, Polish Academy of Sciences, Al. Lotnikow 32/46, 02-668 Varszawa, Poland

*Tel: 00330320434966; Fax: 00330320436591
Email: ydir.androussi@univ-lille1.fr

A Transmission Electron Microscopy study of composition in $Si_{1-x}Ge_x$ / Si (001) quantum dots

Y. ANDROUSSI[1*], T. BENABBAS[1], S. KRET[2], V. FERREIRO[1] and A. LEFEBVRE[1]

[1] Laboratoire de Structure et Propriétés de l'Etat Solide (UMR CNRS 8008), Université des Sciences et Technologies de Lille, Bâtiment C6, 59655 Villeneuve d'Ascq cedex, France

[2] Institute of Physics, Polish Academy of Sciences, Al. Lotnikow 32/46, 02-668 Varszawa, Poland

A finite-element program has been developed to model strain relaxation in the case of epitaxial $Si_{1-x}Ge_x$ / Si coherent quantum dots either with or without compositional inhomogeneities. The resulting elastic displacement fields are used to calculate the intensity of dynamical plan view TEM images of such quantum dots. Various types of linear or parabolic compositional inhomogeneities are studied. TEM images of quantum dots with such inhomogeneities are calculated as well as those of quantum dots with a homogeneous composition. They are then compared with experimental images. It is shown how the analysis of the main features of these experimental images (black/white lobes and moiré-like fringes) enables us to determine the conditions in which it is possible to distinguish quantum dots with a homogeneous composition from those with compositional inhomogeneity.

***Keywords*:** Transmission electron microscopy; quantum dots; chemical composition; displacement field

1. INTRODUCTION

Self-assembled quantum dots (QDs) in heteroepitaxial semiconductor systems have recently been an area of intense study because many electronic devices based on QDs have been theoretically proved to possess better electronic and optical properties than quantum-well devices. Knowing the structural parameters of QDs including the shape, size and chemical composition at different stages of QD island growth is thus important for understanding the structure-property relationship of the QDs as well as revealing information on QD growth mechanisms [1]. However, the accurate characterization of coherent islands is not trivial due to their small sizes and the coupling effects between composition and strain field. An additional complexity is that the island shape and composition are a function of substrate temperature (during growth), of coverage and of the type of crystal growth technique.

Ge/Si (001), in particular, has served as a model system because it is a simple two-component system and due to the hope of combining these QDs easily with existing Si technology. Morphology evolution of uncapped QDs has been extensively investigated and it is reasonably well understood [2-4], but despite its impact on optical and electronic properties, island composition evolution is still in debate. The determination of local composition can be carried out with techniques that average over many islands. These include high resolution x-ray diffraction [5], x-ray anomalous scattering [6,7] and x-ray absorption fine structure [8]. Selective etching coupled with atomic force microscopy [9] and electron-microscope-based methods make it possible to measure composition variations throughout individual islands. These methods are scanning tunneling microscopy [10] and transmission electron microscopy (TEM) techniques including high resolution imaging combined with finite element analysis [11], electron energy loss spectrometry (EELS) [12-14] and x-ray energy dispersive spectrometry (EDS) [15-16]. For each of the above TEM studies, very thin cross-section specimens are required. However, it is difficult to prepare cross-section TEM specimens, especially for samples with low QD densities, and even then the section might include any part of the QD. As a result, there is an advantage in using plan-view samples. Besides, plan-view samples have a larger sampling region that provides a superior statistical basis and contrary to cross-section samples, the surface relaxation effects are negligible in them. That is why plan-view specimens have been successfully used to extract alloying information in $Si_{1-x}Ge_x$/Si QDs from diffraction contrast images [17].

It has been recently shown that information on the chemical composition of coherently strained islands can also be obtained by TEM when fringes - which we have called “moiré-like fringes“- are observed in plan-view images of $In_xGa_{1-x}As$/GaAs QDs [18-20]. The same type of fringes has also been observed in SiGe/Si QDs [21-22]. This paper is aimed at showing that these moiré-like fringes can be used to study the chemical composition of such QDs. Finite-

element (FE) calculations are performed in order to take account of various complex compositional variations. It is then shown how the resulting strain fields (and consequently the compositional inhomogeneities) can be studied via the dynamical contrast of TEM plan-view images of QDs.

2. EXPERIMENTAL PROCEDURE

The growth of the self-assembled islands is carried out in an ultra-vacuum chemical vapor deposition growth chamber with silane and germane diluted in hydrogen used as precursors [23]. Four monolayers of Ge are deposited at 600 or 700°C on Si (001). Atomic force microscopy (AFM) experiments are carried out in air using a Nanoscope III Multimode microscope from Digital Instruments operating in the tapping mode. Integrated silicon tips with a radius of curvature of about 10 nm and cantilevers (model TSEP) with a nominal spring constant 30 Nm^{-1} are used. The (512 x 512 pixels) images are obtained with a 100 x 100 μm piezoelectric scanner and with a 0.4 Hz scanning frequency.

[Insert figure 1 about here]

The finite-element (FE) calculations are performed using a "home-made" program so as to calculate displacement fields **R** taking account of possible compositional variations in $Si_{1-x}Ge_x$/Si QDs. They are carried out in the case of lens-shaped domes (Fig. 1) with values of b and h as indicated in table 1. The compositional variations are introduced by local variations of the elastic constants and for each finite element, a virtual thermal expansion coefficient is introduced so as to simulate a local lattice mismatch that will occur during the FE calculation by raising the temperature by 1K. The thermal expansion coefficient α has thus to fulfill the relation $a(x) = a(0)\ (1 + \alpha\ \Delta T)$ where a(x) is the bulk-material lattice parameter corresponding to the Si concentration x of the finite element.

[Insert table 1 about here]

Plan-view TEM thin foils are mechanically thinned from the substrate side by wedge polishing. TEM images are taken with a Philips CM30 microscope (operated at 300 kV) and directly captured with a cooled slow-scan charge-coupled device (CCD) Gatan camera.

The two-beam dynamical TEM contrast of QDs is simulated by solving the Howie and Whelan equations based on the so-called column approximation [24]. The displacement field **R** is computed at equispaced points in the [001] direction by carrying out the Lagrange interpolation procedure on the data points provided by finite-element calculations. It should be noted that these calculations make it possible to readily vary the shape of the islands and their aspect ratio.

3. RESULTS

A bimodal dot distribution with square-based pyramids and domes is observed by atomic force microscopy at 700°C (see for instance both types of islands in Fig. 2) whereas only domes are observed at 600°C. The average sizes of both types of islands are indicated in table 1 as a function of temperature. The aspect ratio $\rho = 0.20 \pm 0.02$ was found to be constant for all the observed D_2 islands.

[Insert figure 2 about here]

The characteristics of plan-view dynamical TEM dark-field images of strained islands have been fully described in the case of coherently strained $In_xGa_{1-x}As/GaAs$ [19,25] or $Si_{1-x}Ge_x/Si$ islands [21,22]. They all exhibit a black/white contrast, as shown in Fig. 3 and 4 in the case of pyramids (P) grown at 700°C and in the case of domes grown at 600°C (D_1) or 700°C (D_2). When the islands display a sufficiently high aspect ratio (h/b > ~ 0.2), moiré-like fringes are found to be superimposed to the black/white contrast (see D_2 domes in Fig. 4). This is fully consistent with what has been demonstrated in the case of $In_xGa_{1-x}As/GaAs$ islands [19]. These images were obtained for QDs on the electron entrance surface, with a diffraction vector **g** = 220 parallel to the interface and with $w_g = s_g\xi_g = -1.10 \pm 0.05$ (s_g is the deviation parameter and ξ_g the extinction distance). This negative value of w_g was used because it was found to give the highest contrasts and because it was consistent with the general rules established by Katerbau [26] for lattice defects near the specimen surfaces. Following these rules, the contrast of such defects depends on the imaging mode (bright or dark field), on the defect position (near the electron entrance or the electron exit surface of the specimen) and on the sign of w_g. The various cases are summarized in table 2 : for bright-field images, the contrast is reduced (enhanced) for $w_g < 0$ ($w_g > 0$) whatever the defect position. On the contrary, for dark-field images, the reduction (or enhancement) simultaneously depends on the sign of w_g and on the defect position. There is thus an advantage to take dark-field images (rather than bright-field images) either with QDs near the electron entrance (with $w_g<0$) or near the electron exit surface (with $w_g>0$): in both cases, the contrast is enhanced for QDs whereas it is reduced for defects resulting from the specimen thinning on the opposite surface.

[Insert figure 3 about here]
[Insert figure 4 about here]
[Insert table 2 about here]

Uncapped $Si_{1-x}Ge_x/Si$ islands grown either by molecular beam epitaxy or by chemical vapor deposition generally display aspect ratios inferior to ~ 0.3 and two types of compositional heterogeneities. In the first type, a diffuse interface with Si/Ge mixing is observed, the island composition is homogeneous away from the intermixed interface and a laterally constant composition is maintained in the r direction [7,13]. In the second type, the islands contain a Si-rich core

covered with a Ge-rich shell and the composition is not laterally constant [6,17]. It should be noted that a uniform composition has been found in low mismatch $Si_{0.8}Ge_{0.2}$ /Si QDs [27]. Islands grown by liquid phase epitaxy are not taken into account in our study because they display higher aspect ratios (~ 0.5) [28]. We have thus calculated dark-field (220) TEM images of D_2 domes for homogeneous compositions and for two types of composition variations. In the first type, a laterally constant composition is maintained in the r direction (Fig. 5a) whereas compositional gradients are introduced in the z direction either with a linear ("linear/linear" model) or S-shaped profile ("linear/S" model). In the second type, various models have been tested with parabolic contour lines in the (r,z) plane and linear dependence on the z axis ("parabolic/linear" model) (Fig. 5b). The linear (S) dependence of indium composition x as a function of z is indicated in Fig. 5c (d).

[Insert figure 5 about here]

Fig. 6 shows calculated dark-field (220) TEM images of $Si_{1-x}Ge_x$/Si domes with the same geometrical characteristics as D_2 domes and either with a homogeneous composition (with various values of germanium content x) (Fig. 6a) or with the models of compositional inhomogeneities defined in Fig. 5 (Fig. 6b-d). All the images have the same characteristics (i.e.black/white contrast and superimposed moiré-like fringes). L is defined as the distance between the centers of white and black lobes, and σ is defined as the mean periodicity of moiré-like fringes (the periodicity of these fringes is not constant within any experimental or calculated images and that is why σ has been defined as a mean periodicity). A (σ, L/b) diagram can be established for various homogeneous or heterogeneous compositions, and with the following parameters in the case of Fig.7: aspect ratio ρ = 0.20, thin foil thickness t = 349 nm, A_{220} = 0.0315 (the anomalous absorption coefficient), ξ^e_{220} = 62.7 nm (the effective extinction distance of $Si_{0.5}Ge_{0.5}$, calculated using the Vegard's law), w_{220} = -1,10. It should be noted that moiré-like fringes are not found for low values of x (x < ~ 0.4 for homogenous composition and x_I or x_S < ~ 0.6 for heterogeneous compositions). The main result in this figure is that islands with a homogeneous composition can be theoretically unambiguously distinguished from islands with compositional inhomogeneity. However the experimental uncertainties on the measured values of σ and L/b (spread out in the rectangle in Fig.7) make it difficult to distinguish between islands with an homogeneous composition x = 0.4 and islands with a "parabolic/linear" heterogeneous composition.

[Insert figure 6 about here]

We have then considered the influence of the uncertainties with which the above parameters (t, A_{220}, ξ^e_{220}, w_{220} and ρ) can be determined. It is thereafter

Deleted: indium

Deleted: Defining L as the distance between the centres of the white and black lobes, and σ the periodicity of moiré-like fringes for every calculated image, a

Formatted: Font color: Red

Formatted: Font color: Red

Formatted: Font color: Red

Formatted: Font: Symbol

Formatted: Font: Symbol

illustrated in the case of the $(\sigma, L/b)_{hom.}$ points corresponding to homogeneous compositions.

[Insert figure 7 about here]

The anomalous absorption coefficients were respectively taken to be A_{220} = 0.0144 for Si and A_{220}= 0.0485 for Ge: these values were obtained from those calculated at 100 kV [29] or 120 kV [30] by extrapolating to 300 kV, using the analysis by Metherell and Whelan [31]. Vegard's law was used in the case of Si_xGe_{1-x} alloys.

[Insert figure 8 about here]

As an example, Fig. 8 shows the variations of $(\sigma, L/b)_{hom.}$ points as a function of A_{220} varying in the range 0.0144 (Si) - 0.0485 (Ge): inspecting this figure shows that for any $Si_{1-x}Ge_x$/Si alloy, the positions of these points are rather insensitive to the uncertainties with which A_{220} can be calculated.
The influence of w_{220} is depicted in Fig. 9. This figure shows that the experimental error in this parameter (± 0.05) has little influence on the $(\sigma, L/b)_{hom.}$ points, mainly through variations in L.

[Insert figure 9 about here]

The effective extinction distances were respectively taken to be ξ^e_{220} = 74.8 ± 0.02 nm for Si and ξ^e_{220} = 50.7 ± 0.11 nm for Ge in keeping with the calculations of Doyle and Turner [32] or Lu et al [33]. The Vegard's law was used in the case of $Si_{1-x}Ge_x$/Si alloys. Calculations show that the positions of $(\sigma, L/b)_{hom.}$ points are insensitive to the uncertainties with which ξ^e_{220} can be calculated.

[Insert figure 10 about here]
[Insert figure 11 about here]

Calculated dark-field (220) TEM contrasts were found to be very dependent on foil thickness t. Defining the moiré-like fringe contrast C as $I_2 - I_1 / I_2 + I_1$ where $I_{2(1)}$ is the intensity of the first dark (bright) fringe in the dark lobe, Fig. 10 shows, for instance in the Si case, that the variation of C as a function of t is periodic and with an approximate ξ^e_{220} period. Only experimental images with the highest contrasts (> ~ 0.50) leading to precise measurements of σ and L, were considered, i.e. images corresponding to the range 330-360 nm for the 300-380 nm period. The specimen thickness was measured in the vicinity of every studied QD and the location of the corresponding electron microprobe was subsequently checked with the resulting contamination spot. As an example, for t = 349 nm situated in this range, Fig. 11 shows the variations of $(\sigma, L/b)_{hom.}$

points corresponding to the uncertainty ± 4 nm with which t can be measured using conventional CBED analysis[34,35]. The influence of this uncertainty on $(\sigma, L/b)_{hom.}$ points is found to be negligible.

[Insert figure 12 about here]

Fig. 12 shows the variations of $(\sigma, L/b)_{hom.}$ points as a function of aspect ratio ($0.15 < \rho < 0.30$). Examining this figure shows that for a homogeneous $x = 0.4$ composition, moiré-like fringes are not found with $\rho = 0.15$, which is consistent with the fact that moiré-like fringes are never observed in the case of D_1 domes. It should be noted that for any given composition x, σ is very sensitive to the variations of ρ and that it is thus important to determine the aspect ratio as accurately as possible. In the case of D_2 domes, the effect of the uncertainty ± 0.02 on the determination of ρ is illustrated in Fig.12.

4. DISCUSSION AND CONCLUSION

The above analysis shows that all the parameters (t, A_{220}, ξ^e_{220}, w_{220} and ρ) influencing the contrast of moiré-like fringes can be measured or calculated with a sufficient precision and have thus little influence on the *calculated* values of σ and L/b. However, the experimental uncertainties on the *measured* values of σ and L/b (spread out in the rectangle in Fig.7-9 and 11-12) make it difficult to distinguish between islands with a homogeneous $x = 0.4$ composition and islands with a "parabolic/linear" heterogeneous composition. That is why an additional x-ray energy dispersive spectrometry investigation has been performed [36] and it has shown that D_2 domes have an approximately homogeneous $x = 0.4$ composition.

This result is consistent with those of Schülli et al [7] who have studied the influence of growth temperature on interdiffusion in uncapped SiGe/Si islands grown by molecular beam epitaxy: the aspect ratio is found to be constant (0.22) between 620 et 750°C and the maximum Ge content rapidly decreases from about 70 to 22% for growth temperatures between 620 and 800°C and is approximately 45% at 700°C.

Our geometrical approach shows how it is possible to distinguish quantum dots with a homogeneous composition from those with compositional inhomogeneity. However this does not make it possible to choose between various compositional variations and precise determination of these variations should take account of the relative intensities of black/white lobes and of moiré-like fringes.

ACKNOWLEDGEMENTS

This work was partially supported by the French " Région Nord-Pas de Calais", by the European FEDER ("Fonds Européen de Développement Régional") and the "Action Concertée Nanosciences/Nanotechnologies". Many thanks are due to

Drs D. Bouchier and L.H. Nguyen (Institut d'Electronique Fondamentale, Orsay, France) for providing the SiGe/Si samples.

REFERENCES

[1] K. Leonardi, H. Heinke, K. Okhawa, D. Hommel, H. Selke, F. Gindele and U. Woggon, Appl. Phys. Lett. **71**, 1510 (1997).

[2] M. Tomitori, K. Watanabe, M. Kobayashi and O. Nishikawa, Appl. Surf. Sci. **76/77**, 322 (1994).

[3] G. Medeiros-Ribeiro, A.M. Bratkowski, T.I. Kamins, D.A. Ohlberg and R.S. Williams, Science **279**, 353 (1998).

[4] S.A. Chaparro, Y. Zhang, J. Drucker, D. Chandrasekhar and D.J. Smith, J. Appl. Phys. **87**, 2245 (2000).

[5] M. Hanke, M. Schmidbauer, R. Köhler, F. Syrowatka, A.K. Gerlitzke and T. Boeck, Appl. Phys. Lett. **84**, 5228 (2004).

[6] A. Malachias, S. Kycia, G. Medeiros-Ribeiro, R. Magalhaes-Paniago, T.I. Kamins and R. S. Williams, Phys. Rev. Lett**. 91**, 176101 (2003).

[7] T.U. Schülli, M. Stoffel, A. Hesse, J. Stangl, R.T. Lechner, E. Wintersberger, M. Sztucki, T.H. Metzger, O.G. Schmidt and G. Bauer, Phys. Rev. B **71**, 35326 (2005).

[8] A. V. Kolobov, H. Oyanagi, S. Wei, K. Brunner, G. Abstreiter and K. Tanaka, Phys. Rev. B **66**, 75319 (2002).

[9] U. Denker, M. Stoffel and O.G. Schmidt, Phys. Rev. Lett. **90**, 196102 (2003).

[10] N. Liu, J. Tersoff, O. Blakenov, A. L. Holmes, Jr. and C.K. Shih, Phys. Rev. Lett. **84**, 334 (2000).

[11] A. Rosenauer, U. Fischer, D. Gerthsen and A. Förster, Appl. Phys. Lett. **71**, 3868 (1997).

[12] T. Walther, C.J. Humphreys and A. G. Cullis, Appl. Phys. Lett. **71**, 809 (1997).

[13] M. Floyd, Y. Zang, K.P. Driver, J. Drucker, P.A. Crozier and D.J. Smith, Appl. Phys. Lett. **82**, 1473 (2003).

[14] H. Kirmse, R. Schneider, R. Otto, W. Neumann, M. Hanke, M. Schmidbauer, R. Köhler, H. Wawra, T. Boeck, I.P. Soshnikov, N.N. Ledentsov, Z.N. Krasilnik and A. Novikov, Inst. Phys. Conf. Ser. No **180**, 115 (2004).

[15] S.A. Chaparro, J. Drucker, Y. Zhang, D. Chandrasekhar, M.R. Mc Cartney and D.J. Smith, Phys. Rev. Lett. **83**, 1199 (1999).

[16] X.Z. Liao, J. Zou, X.F. Duan, D.J.H. Cockayne, Z.M. Jiang, X. Wang and R. Leon, Appl. Phys. Lett. **77**, 1304 (2000).

[17] X.Z. Liao, J. Zou, D.J.H. Cockayne, Z.M. Jiang, and X. Wang, J. Appl. Phys. **90**, 2725 (2001).

[18] Y. Androussi, D. Ferré and A. Lefebvre, Appl. Surf. Sci. **117**, 258 (2001).

[19] Y. Androussi, T. Benabbas and A. Lefebvre, Ultramicr. **93**, 161 (2002).

[20] Y. Androussi, T. Benabbas, D. Jacob and A. Lefebvre, Inst. Phys. Conf. Ser. No **180,** 95 (2004).

[21] P.D. Miller, C.P. Liu, W.L. Henstrom, J.M. Gibson, D.G. Cahill, Y. Huang, P. Zhang, T.I. Kamins, D.P. Basile and R.S. Williams, Appl. Phys. Lett. **75**, 46 (1999).

[22] P.D. Miller, C.P. Liu and J.M. Gibson, Ultramicr. **84**, 225 (2000).

[23] P. Boucaud, V. Le Thanh, V. Yam, S. Sauvage, N. Meneceur, M. Elkurdi, D. Débarre and D. Bouchier, Mat. Sci. Eng. B **89**, 36 (2002).

[24] P.B. Hirsch, A. Howie, R.B. Nicholson, R.B. Pashley and M.J. Whelan, *Electron Microscopy of Thin Crystal* (Butterworths, London, 1977).

[25] T. Benabbas, P. François, Y. Androussi and A.Lefebvre A, J. Appl. Phys. **80**, 2763 (1996).

[26] K.H. Katerbau, Phil. Mag. **43**, 409 (1981).

[27] J.A. Floro, E. Chason, L.B. Freund, R.D. Twesten, R.Q. Hwang and G.A. Lucadamo, Phys. Rev. B**59**, 1990 (1999).

[28] M. Hanke, M. Schmidbauer, R. Köhler, F. Syrowatka, A.K. Gerlitzke and T. Boeck, Appl. Phys. Lett. **84**, 5228 (2004).

[29] G. Radi, Acta Cryst. **A26**, 41 (1970).

[30] S. Swaminathan, S. Altynov, I.P. Jones, N.J. Zaluzec, D.M. Maher and H.L. Fraser, Ultramicr. **69**, 169 (1997).

[31] J.F. Metherell and M.J. Whelan, Phil. Mag. **15**, 755 (1967).

[32] P.A. Doyle and P.S. Turner, Acta Cryst. A**24**, 390 (1968).

[33] Z.W. Lu, A. Zunger and M. Deutsch, Phys. Rev. **B47**, 9385 (1993).

[34] P.M. Kelly, A. Jostsons, A.G. Blake and J.G. Napier, Phys. Stat. Sol (a) **31**, 771 (1975).

[35] D. Delille, R. Pantel and E. Van Cappellen, Ultramicr. **87**, 5 (2001).

[36] D. Brouri, J.Y. Laval, M. Zak and C. Delamarre, unpublished results.

Growth temperature (°C)	b (nm)	h (nm)
600	100 (D_1)	15 (D_1)
700	110 (D_2) 100 (P)	22 (D_2) 12 (P)

Table 1: Average sizes of domes (D_1 and D_2) and pyramidal islands (P) for various growth temperatures ; b=base, h= height.

	Electron entrance surface	Electron exit surface
Bright field		
$w > 0$	+	+
$w < 0$	-	-
Dark field		
$w > 0$	-	+
$w < 0$	+	-

Table 2: Enhancement (+) or reduction (-) of dynamical TEM contrast for lattice defects near the specimen surfaces.

Figure captions

Figure 1: Schematic view of the dome-shaped islands used for the FE calculations and for the TEM contrast simulations.

Figure 2: Tapping mode (1.2 µm x 1.2 µm) image of $Si_{1-x}Ge_x$/Si QDs grown at 700°C. A few pyramidal (dome-shaped) QDs are indicated with black (white) arrows.

Figure 3: Experimental dark-field (220) TEM image of D_1 dome-shaped $Si_{1-x}Ge_x$/Si QDs grown at 600°C; w_{220} = -1.10.

Figure 4: Experimental dark-field (220) TEM image of $Si_{1-x}Ge_x$/Si QDs grown at 700°C; w_{220} = -1.10, t = 349 nm. (a): a pyramid (P) and two domes (D_2 and D'_2). Only the domes display moiré-like fringes. (b): enlargement of the D_2 dome.

Figure 5: Various models of compositional inhomogeneity. (a): linear variation in the (r,z) plane. (b): parabolic variation in the (r,z) plane. (c): linear dependence of germanium composition x as a function of z and for r = 0. (d): S dependence of germanium composition x as a function of z and for r = 0.

Deleted: indium

Deleted: indium

Figure 6: Calculated dark-field (220) TEM images of dome-shaped $Si_{1-x}Ge_x$/Si QDs with a homogeneous composition (a), or with various compositional inhomogeneities: linear/linear model (b), linear/S model (c), parabolic/linear

model (d). Aspect ratio ρ = 0.20, t = 349 nm, A_{220} = 0.0315, ξ^{e}_{220} = 62.7 nm, w_{220} = -1,10.

Figure 7: Calculated (σ, L/b) diagram for dome-shaped $Si_{1-x}Ge_x$/Si QDs, either with homogeneous compositions and various x silicon contents (◆) or with compositional inhomogeneities: (■) = linear/linear model; (▲) = linear/S model; (□) = parabolic/linear model. Aspect ratio ρ = 0.20, t = 349 nm, A_{220} = 0.0315, ξ^{e}_{220} = 62.7 nm, w_{220} = -1,10. Experimental points corresponding to the measured values σ and L/b are spread out into the rectangle located in the upper part of the figure.

Figure 8: Variations of $(\sigma, L/b)_{hom.}$ points as a function of A_{220}. Aspect ratio ρ = 0.20, t = 349 nm, ξ^{e}_{220} = 62.7 nm, w_{220} = -1,10. The rectangle located in the upper part is the same as in Fig.7.

Figure 9: Variations of $(\sigma, L/b)_{hom.}$ points for various values of w_{220} corresponding to the experimental uncertainties. Aspect ratio ρ = 0.20, t = 349 nm, A_{220} = 0.0315, ξ^{e}_{220} = 62.7 nm. The rectangle located in the upper part is the same as in Fig.7.

Figure 10: Moiré-like fringe contrast C as a function of the foil thickness t. Aspect ratio $\rho = 0.20$, $A_{220} = 0.0315$, $\xi^{e}_{220} = 62.7$ nm, $w_{220} = -1{,}10$.

Figure 11: Variations of $(\sigma, L/b)_{hom.}$ points for various values of t ranging from 345 to 353 nm. Aspect ratio $\rho = 0.20$, $A_{220} = 0.0315$, $\xi^{e}_{220} = 62.7$ nm, $w_{220} = -1{,}10$. The rectangle located in the upper part is the same as in Fig.7.

Figure 12: Variations of $(\sigma, L/b)_{hom.}$ points for various values of ρ ranging from 0.15 to 0.30: (◆) $\rho = 0.15$; (■) $\rho = 0.20$; (▲) $\rho = 0.25$; (●) $\rho = 0.30$. $A_{220} = 0.0315$, $\xi^{e}_{220} = 62.7$ nm, $w_{220} = -1{,}10$, t = 349 nm. The rectangle located in the upper part is the same as in Fig.7. The effect of the uncertainty ± 0.02 with which $\rho = 0.20$ can be measured is illustrated with dotted rectangles.

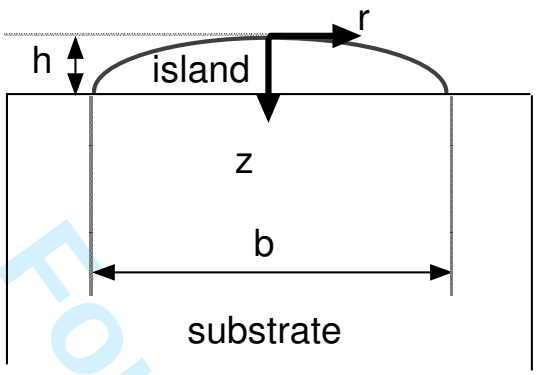

Figure 1

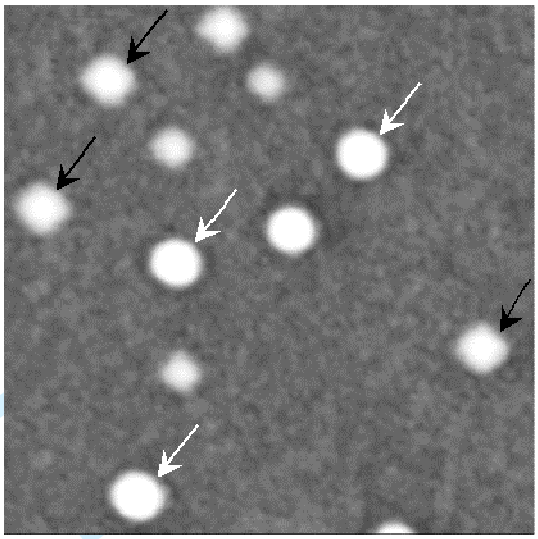

Figure 2

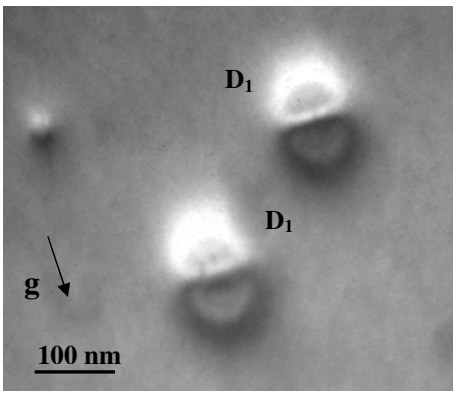

Figure 3

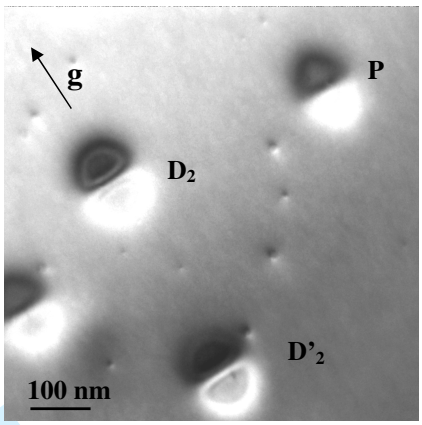

a

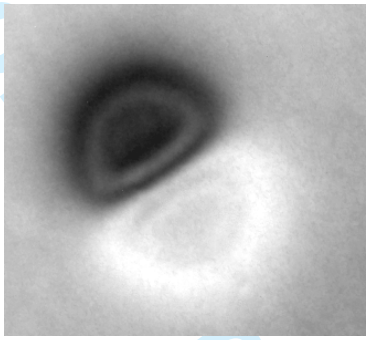

b

Figure 4

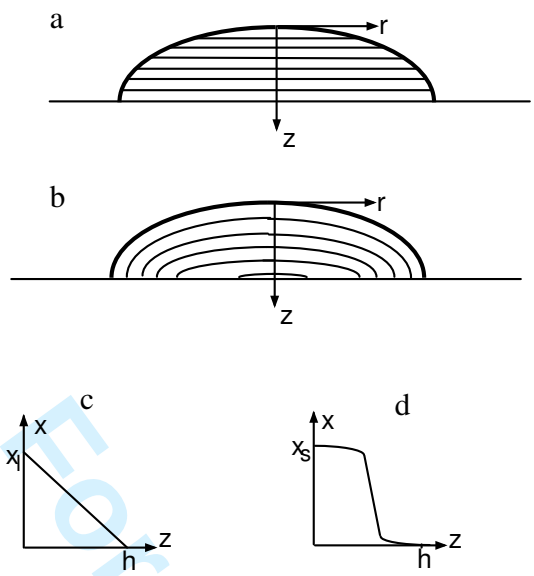

Figure 5

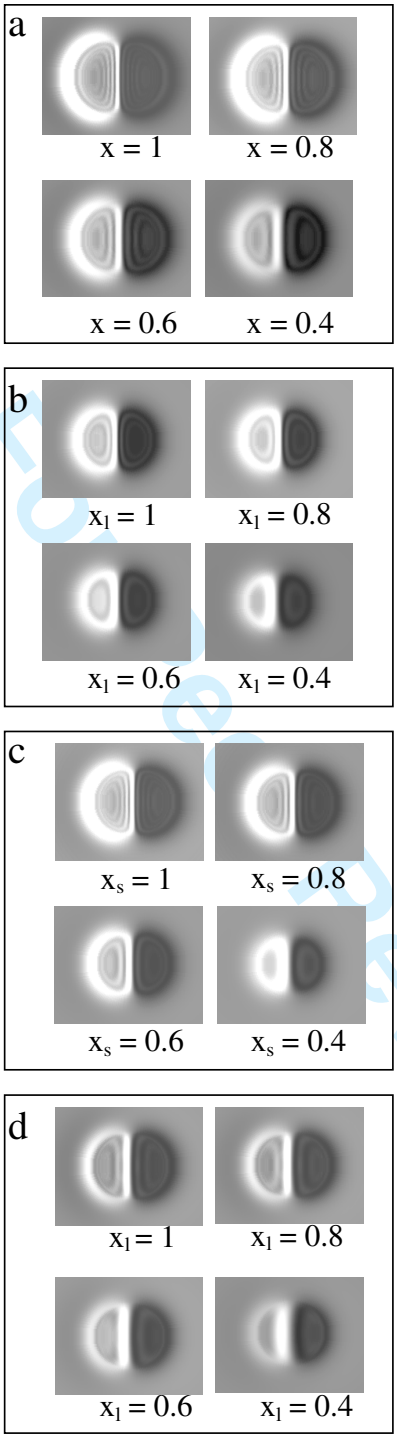

Figure 6

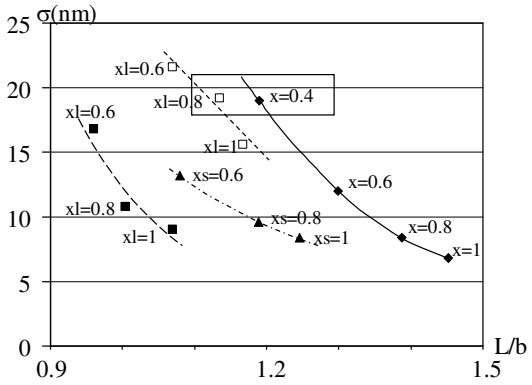

Figure 7

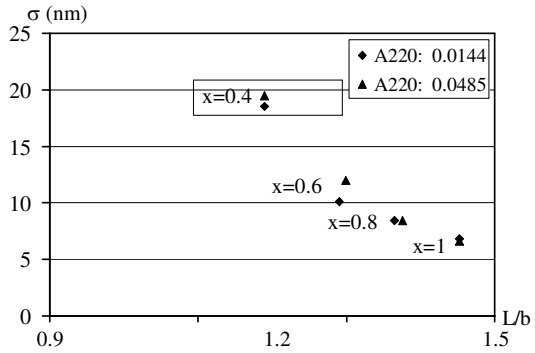

Figure 8

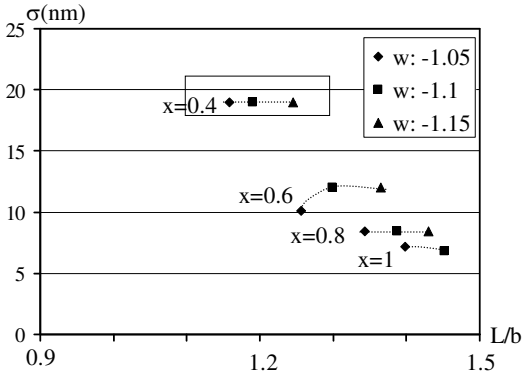

Figure 9

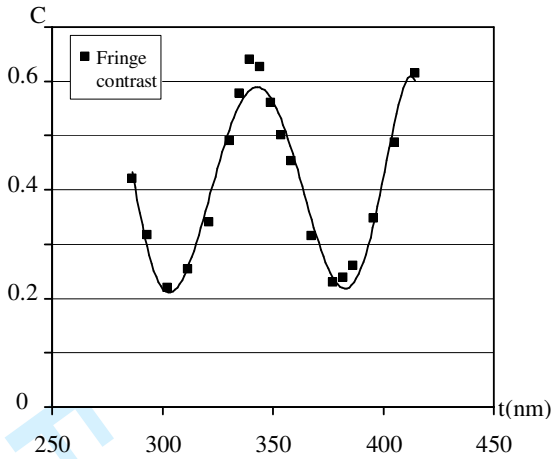

Figure 10

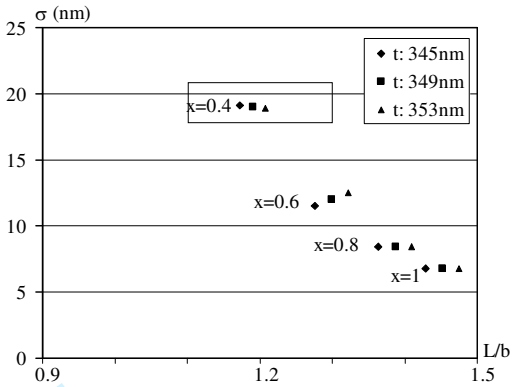

Figure 11

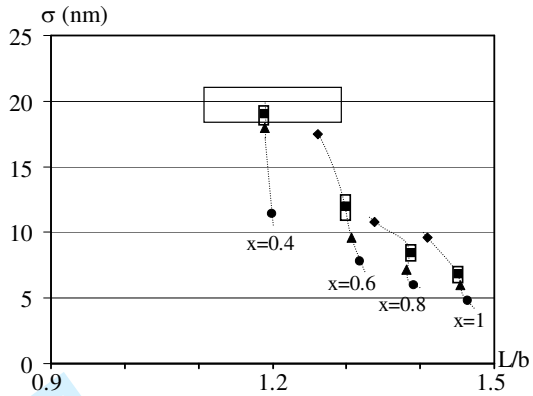

Figure 12